

Lab

Dyson Lewis
UCLA / ASTR 180
November 23, 2025

Abstract

We present a photometric analysis of the open cluster NGC 6791 using archival *HST*/WFC3 UVIS imaging in the F606W and F814W filters. Aperture photometry was calibrated to the Vega system using standard WFC3 zeropoints, allowing us to construct color–magnitude diagrams and identify main-sequence stars via iterative ridge-line fitting with 3σ outlier rejection. Our catalog contains ~ 950 stars with reliable photometry (magnitude errors < 0.15 mag, color errors < 0.25 mag), of which ~ 500 were classified as main-sequence members. By comparing our main sequence to that of M15 at a known distance of 9.98 ± 0.47 kpc, we derived a distance modulus of $\mu = 12.27 \pm 0.49$ mag, corresponding to a distance of $d = 2.84 \pm 0.64$ kpc for NGC 6791. Including bright stars with adaptive apertures versus restricting the fit to faint stars produced consistent distance estimates due to the stability of the ridge line across the fitted magnitude range.

Keywords: Open Clusters, Color-Magnitude Diagrams, Photometry, Distance Determination, HST, NGC 6791

1 Introduction

Accurate distance measurements are essential for characterizing stellar systems and understanding Galactic structure. One of the most effective methods for determining distances to star clusters is the color–magnitude diagram (CMD), which plots stellar brightness against color. By comparing the apparent main sequence of a target cluster to that of a reference cluster with known distance, the vertical offset between the two sequences yields the distance modulus. This relies on the fact that main-sequence stars of similar color (and therefore temperature and spectral type) share similar absolute magnitudes.

The relation between apparent magnitude m , absolute magnitude M , and distance d (in parsecs) is

$$\mu = m - M = 5 \log_{10}(d) - 5, \quad (1)$$

which forms the basis of our distance determination.

NGC 6791 is an unusually old and metal-rich open cluster located in Lyra at (RA, Dec) = ($19^h 20m 52.8s$, $+37^\circ 46' 40''$) (J2000). With an age of ~ 8 Gyr and metallicity $[Fe/H] \approx 0.4$, it is among the most metal-rich open clusters known and has been studied extensively across the electromagnetic spectrum. Recent Gaia DR3 analyses by Ahmed (2025) yielded a distance modulus of $\mu = 13.1 \pm 0.08$ mag (distance 4170 ± 262 pc), along with updated proper motions and membership probabilities.

In this study, we determine the distance to NGC 6791 using archival *HST*/WFC3 UVIS imaging in the F606W and F814W filters, approximating the Johnson *V* and *I* bands. Figure 1 shows the processed *HST*/WFC3 images in F606W and F814W. Invalid pixels from the drizzling pipeline (NaNs and negatives) have been removed, and these cleaned images form the basis for our stellar photometry. Our analysis focuses on a region $57''$ from the cluster center. After performing aperture photometry and constructing CMDs, we compare the cluster’s main sequence to that of the globular cluster M15, whose distance is well measured at 9.98 ± 0.47 kpc. The magnitude offset at fixed color provides the distance modulus and thus the distance to NGC 6791.

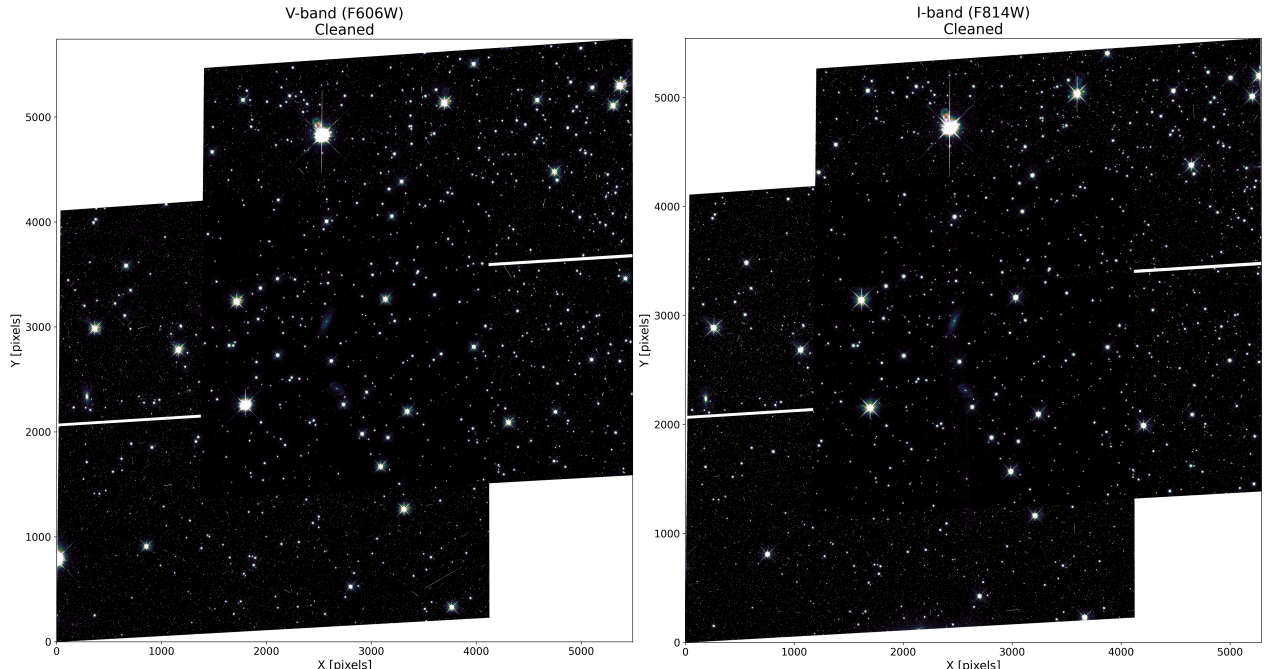


Figure 1: Processed *HST*/WFC3 UVIS images of the NGC 6791 field. Left: F606W (V-band equivalent). Right: F814W (I-band equivalent).

2 Observations & Data Reduction

2.1 Data Acquisition

Observations of NGC 6791 were obtained from the Mikulski Archive for Space Telescopes (MAST) using archival *HST/WFC3 UVIS* imaging. The dataset consists of drizzled images in two broadband filters: F606W (exposure time 844 s) and F814W (exposure time 1426 s), which approximate the Johnson *V* and *I* bands, respectively. The downloaded images had already undergone standard calibration steps: bias subtraction (BIASCORR), dark current correction (DARKCORR), flat-fielding (FLATCORR), charge-transfer efficiency correction (PCTECORR), and drizzle combination (DRIZCORR). These pipeline reductions remove the need for standard CCD processing typically required for ground-based observations.

2.2 Initial Image Processing

The drizzled images contain NaN values near the edges where the dithered exposures do not fully overlap. To enable automated star detection across the full field, we applied a median-replacement algorithm using the `median_replace` function, which substitutes NaN pixels with values interpolated from a local median filter. Remaining negative pixel values, arising from the drizzling process, were set to near-zero. This cleaning procedure produced continuous images suitable for photometric analysis while preserving stellar flux integrity.

2.3 Star Detection Pipeline

We implemented a two-tier detection pipeline to accommodate the wide dynamic range of stellar brightnesses in the field.

Bright Star Detection: Bright stars were first identified using `detect_bright_stars_initial`, which applies Gaussian smoothing ($\sigma = 4.5$ pixels) followed by maximum filtering to isolate local maxima above a flux threshold. These preliminary detections were refined with `refine_bright_stars`, which extracts a cutout around each candidate, performs local sky subtraction using edge pixels, and computes intensity-weighted centroids via `find_star_center`:

$$x_c = \frac{\sum_i I_i x_i}{\sum_i I_i}, \quad y_c = \frac{\sum_i I_i y_i}{\sum_i I_i} \quad (2)$$

where I_i is the intensity of pixel i and (x_i, y_i) are its coordinates, with the sum taken over all pixels exceeding the 90th percentile brightness threshold. To prevent diffraction spikes from biasing the radius measurement, stellar radii are estimated using three independent methods applied to the radial brightness profile (computed in 0.5-pixel annular bins using the median for robustness):

1. **Flux threshold:** The radius at which the profile drops below 3% of the peak flux for three consecutive bins.
2. **Gradient analysis:** The radius at which a large negative gradient (indicating the stellar edge) is followed by a plateau or increase (indicating spike contamination), detected when $\nabla I < -\frac{I_{\text{peak}}}{2r_{\max}}$ and $\langle \nabla I \rangle_{j+1:j+4} > 0.3 \nabla I_j$.
3. **Signal-to-noise:** The radius at which the profile drops below $2.5\sigma_{\text{sky}}$ for three consecutive bins.

The final radius is determined by computing pairwise differences among the three estimates and averaging the two most consistent values. If all three methods agree within 5 pixels, the median is used instead. This consensus approach minimizes bias from any single method that may be affected by spike contamination. The combined estimate is then blended with the raw radius from `find_star_center` (weighted 40% raw, 60% consensus) if the raw value is reasonable, and finally clipped to the range $[r_{\min}, r_{\max}] = [5, 25]$ pixels.

Quality checks reject candidates whose refined center moved more than half the box size from the initial position, whose peak brightness falls below 30 counts, or whose position lies within 40 pixels of an already-accepted star. An illustrative example of a bright star, including its diffraction spikes and derived apertures, is shown in Figure 2.

Diffraction Spike Detection and Removal: Prominent diffraction spikes in *HST* images arise from the telescope’s secondary mirror support structure and appear as linear vertical and horizontal features. For the brightest stars, saturation can amplify these artifacts. We developed an algorithm `fit_diffraction_spikes` to detect and remove such features by searching for chains of aligned detections along each axis within a search width proportional to the bright star’s radius. Candidate spike segments with separations less than 30 pixels and containing two or more aligned detections were flagged using the Modified Z-Score statistic:

$$M_i = \frac{0.6745 \times (F_i - \tilde{F})}{\text{MAD}} \quad (3)$$

where F_i is the measured flux for source i , \tilde{F} is the median flux, and MAD is the Median Absolute Deviation. Sources with $|M_i| > 3.8$ were flagged as potential spike artifacts, and all but the brightest source in each segment were removed. Diagonal spikes from HST’s four-vane spider are not explicitly fitted but are typically fainter and contribute few false detections.

Faint Star Detection: After masking bright stars and their associated spike artifacts, faint sources were detected using `detect_faint_stars`. Adaptive masks extending to $2\times$ each bright star’s radius were applied, after which peak detection was performed in the remaining unmasked regions using Gaussian smoothing ($\sigma = 1.5$ pixels) and a lower flux threshold. The final distribution of faint and bright detections in the F606W frame is shown in Figure 3.

The full detection pipeline identified 31 bright stars and 2053 faint stars in F606W, with 150 spike artifacts removed. In F814W, 13 bright stars and 1594 faint stars were detected, with 129 identified spike artifacts removed.

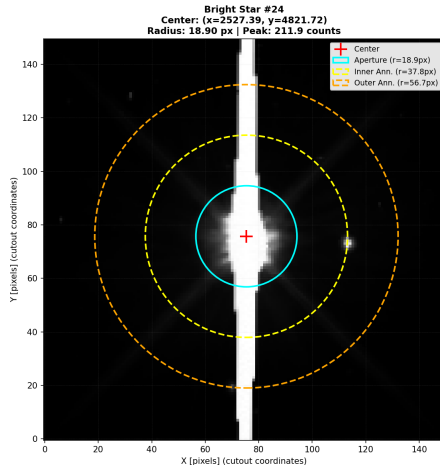


Figure 2: Example of the brightest detected star in the F606W image. The cyan circle shows the photometric aperture, yellow dashed circles mark the inner and outer sky annulus boundaries, and the red cross indicates the measured centroid. The linear features extending vertically and horizontally from the star are diffraction spikes, which must be accounted for in the detection pipeline.

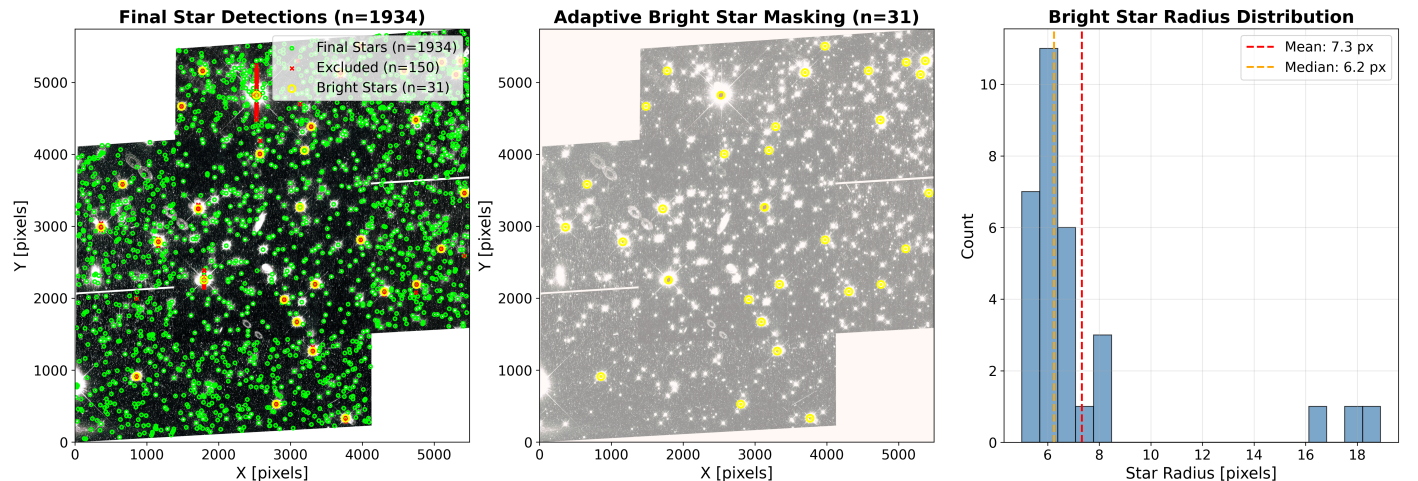


Figure 3: Star detection results for the F606W image. Left: overlay of all detected stars (green dots). Middle: overlay showing only the brightest stars (yellow circles). Right: histogram of measured radii for the brightest stars.

2.4 Aperture Photometry

Photometry was performed using `ap_phot`, which implements circular aperture photometry with fractional pixel weighting. For faint stars, we used a fixed circular aperture of radius 1.5 pixels and a sky annulus from 5 to 10 pixels. For bright stars, we used adaptive apertures scaled to each star's measured radius: the photometric aperture radius was set equal to the stellar radius, and the sky annulus spanned $2\times$ to $3\times$ that radius.

The sky-subtracted flux was computed as:

$$F = \sum_i w_i I_i - \bar{I}_{\text{sky}} \sum_i w_i \quad (4)$$

where w_i is the fractional pixel weight (the overlap fraction between pixel i and the circular aperture), I_i is the pixel intensity in DN, and \bar{I}_{sky} is the mean sky background per pixel estimated from the median of the sky annulus.

Photometric uncertainties were computed as:

$$\sigma_F = \sqrt{\frac{F}{g} + n_{\text{ap}} \sigma_{\text{sky}}^2 + \frac{n_{\text{ap}}^2 \sigma_{\text{sky}}^2}{n_{\text{ann}}}} \quad (5)$$

where g is the detector gain, $n_{\text{ap}} = \sum_i w_i$ is the effective number of pixels in the aperture, σ_{sky}^2 is the variance of pixel values in the sky annulus, and n_{ann} is the number of pixels in the sky annulus. The three terms represent Poisson noise from the source, sky background variance within the aperture, and uncertainty in the mean sky level, respectively.

2.5 Photometric Calibration

Instrumental fluxes in electrons per second were converted to Vega magnitudes using the WFC3/UVIS zeropoints from STScI: $ZP_{F606W} = 26.0039 \pm 0.0129$ mag and $ZP_{F814W} = 24.6985 \pm 0.0075$ mag. Magnitudes were computed using

$$m = -2.5 \log_{10}(F) + ZP, \quad (6)$$

where F is the measured flux (e s^{-1}). Magnitude uncertainties were propagated as:

$$\sigma_m = \sqrt{\left(\frac{2.5}{\ln 10} \frac{\sigma_F}{F}\right)^2 + \sigma_{ZP}^2} \quad (7)$$

A full list of time-dependent WFC3 UVIS inverse sensitivities and zero points can be found in Calamida et al. (2021).

2.6 Band Alignment and Star Matching

The F606W and F814W images have slight pointing offsets. We computed the coordinate offset using `find_offset_from_bright_stars`, which cross-matches the 20 brightest stars in each frame and measures the median positional difference:

$$\Delta x = \text{median}(x_{I,i} - x_{V,i}), \quad \Delta y = \text{median}(y_{I,i} - y_{V,i}) \quad (8)$$

where $(x_{V,i}, y_{V,i})$ and $(x_{I,i}, y_{I,i})$ are the matched bright star positions in the F606W and F814W frames, respectively.

After applying the offset to align the coordinate systems, stars were matched between bands using the `match_stars` function, which employs a KD-tree algorithm for efficient nearest-neighbor searching. A KD-tree was constructed from the F606W star positions, and for each F814W star, the nearest F606W neighbor was identified by querying the tree. Only pairs with separations less than the matching tolerance of 3 pixels (d_{tol}) were retained:

$$d_{ij} = \sqrt{(x_{V,i} - x_{I,j})^2 + (y_{V,i} - y_{I,j})^2} < d_{\text{tol}} \quad (9)$$

This approach provides $\mathcal{O}(n \log n)$ computational efficiency compared to brute-force matching with $\mathcal{O}(n^2)$.

For each matched star, the color index was computed as:

$$(V - I) = m_{\text{F606W}} - m_{\text{F814W}} \quad (10)$$

with uncertainties propagated as:

$$\sigma_{(V-I)} = \sqrt{\sigma_V^2 + \sigma_I^2} \quad (11)$$

2.7 Quality Filtering

To ensure reliable CMD photometry, we applied cuts requiring magnitude uncertainties < 0.15 mag in both bands and color uncertainties < 0.25 mag. This removed low-S/N sources and stars affected by crowding or edge artifacts. The full analysis was performed twice—first using only faint stars, and then including bright stars with adaptive apertures—to test whether bright-star inclusion affects the derived cluster distance.

2.8 Main Sequence Fitting

Main sequence stars were identified using the iterative ridge-line fitting procedure of McNamara et al. (2004). An initial CMD selection box spanned $19.0 < V < 22.0$, $18.0 < I < 20.5$ and $0.5 < (V - I) < 1.5$. Median colors were computed in 0.4 mag bins and fit with a fourth-order polynomial to define an initial ridge line. Stars were rejected if their color deviation exceeded 3σ :

$$|(V - I)_{\text{obs}} - (V - I)_{\text{ridge}}(V)| > 3\sigma_{\text{color}}(V) \quad (12)$$

where $(V - I)_{\text{ridge}}(V)$ is the polynomial ridge-line color at magnitude V , and $\sigma_{\text{color}}(V)$ is the mean absolute deviation of colors in that magnitude bin. The polynomial was refit iteratively until convergence, and the final ridge line defines the main sequence locus.

2.9 Distance Modulus Measurement

To determine the distance to NGC 6791, we compared our main sequence to that of the reference cluster M15, which has a well-established distance of 9.98 ± 0.47 kpc (McNamara et al., 2004). We adopted $(V - I) = 0.8$ as the reference color, well within the main sequence of both clusters and away from the turnoff or giant branch.

The reference V magnitude at this color for M15 was taken from the CMD in Houdashelt et al. (2001), where $V \approx 22.5 \pm 0.25$ mag by visual interpolation. For NGC 6791, the ridge-line magnitude at the same color was obtained from our polynomial fit, and local scatter was assessed using stars within ± 0.05 mag in color.

The distance modulus was computed using

$$\mu_{\text{NGC}6791} = V_{\text{NGC}6791} - V_{\text{M15}} + \mu_{\text{M15}}, \quad (13)$$

where $\mu_{\text{M15}} = 14.996 \pm 0.102$ mag. The distance to NGC 6791 was then calculated from the distance modulus relation:

$$d_{\text{NGC}6791} = 10^{(\mu_{\text{NGC}6791}+5)/5} \text{ pc.} \quad (14)$$

3 Results

3.1 Photometric Catalog

Table 1 summarizes the photometric extraction results for both the faint-only and faint+bright analyses. After aperture photometry in each band, stars were cross-matched between the F606W and F814W images using a coordinate offset of $(-101.127 \pm 0.016, -99.635 \pm 0.348)$ pixels determined from bright star positions.

Table 1: Photometric Extraction Summary

Parameter	Faint Only	Faint + Bright
Input stars (V-band)	2053	2084
Input stars (I-band)	1594	1607
Valid photometry (V)	1995	2026
Valid photometry (I)	1558	1571
Edge rejections (V/I)	2 / 2	2 / 2
NaN rejections (V/I)	12 / 9	12 / 9
Negative flux (V/I)	44 / 25	44 / 25
Cross-matched stars	957	986
V magnitude range (mag)	18.04 – 26.93	13.45 – 26.93
I magnitude range (mag)	17.50 – 25.71	13.31 – 25.71
Color (V–I) range (mag)	–0.05 – 2.43	–2.71 – 2.43

Of the initial detections, approximately 97% yielded valid photometric measurements, with the small number of rejections primarily due to negative flux values (44 in V-band, 25 in I-band) likely caused by sources falling on noisy pixels or near image artifacts. The cross-matching process successfully paired 957 stars between bands in the faint-only analysis and 986 stars when including bright sources. The extended magnitude range in the faint+bright dataset (reaching $V = 13.45$ compared to $V = 18.04$) demonstrates successful recovery of the brightest cluster members using adaptive apertures. The broader color range (–2.71 to 2.43 mag vs. –0.05 to 2.43 mag) reflects the inclusion of bright blue horizontal branch stars that were excluded from the faint-only sample.

Quality filtering based on photometric uncertainties was applied to both datasets. Table 2 presents the filtering results and error statistics for the final catalogs used in CMD analysis.

Table 2: Quality Filtering and Error Statistics

Parameter	Faint Only	Faint + Bright
Total matched stars	957	986
Stars passing quality cuts	927 (96.9%)	953 (96.7%)
Rejected stars	30 (3.1%)	33 (3.3%)
Mean V error (mag)	0.0285	0.0285
Mean I error (mag)	0.0226	0.0245
Mean color error (mag)	0.0374	0.0391
Additional stars from bright	—	+26

The inclusion of bright stars with adaptive aperture photometry added 26 matched sources passing quality filtering. Both datasets show comparable mean photometric errors, indicating reliable recovery of bright star photometry. The slightly higher I-band error in the faint+bright dataset (0.0245 vs. 0.0226 mag) reflects the inclusion of bright stars where saturation effects may introduce additional uncertainty, though this difference is negligible for our analysis. The near-identical rejection rates (3.1% vs. 3.3%) confirm that the adaptive aperture technique does not systematically degrade photometric quality for bright sources.

3.2 Color-Magnitude Diagrams

Figure 4 presents the color–magnitude diagrams for both datasets prior to main-sequence fitting, comparing the faint-only analysis (left column) with the faint+bright analysis (right column) in both V-band (top row) and I-band (bottom row).

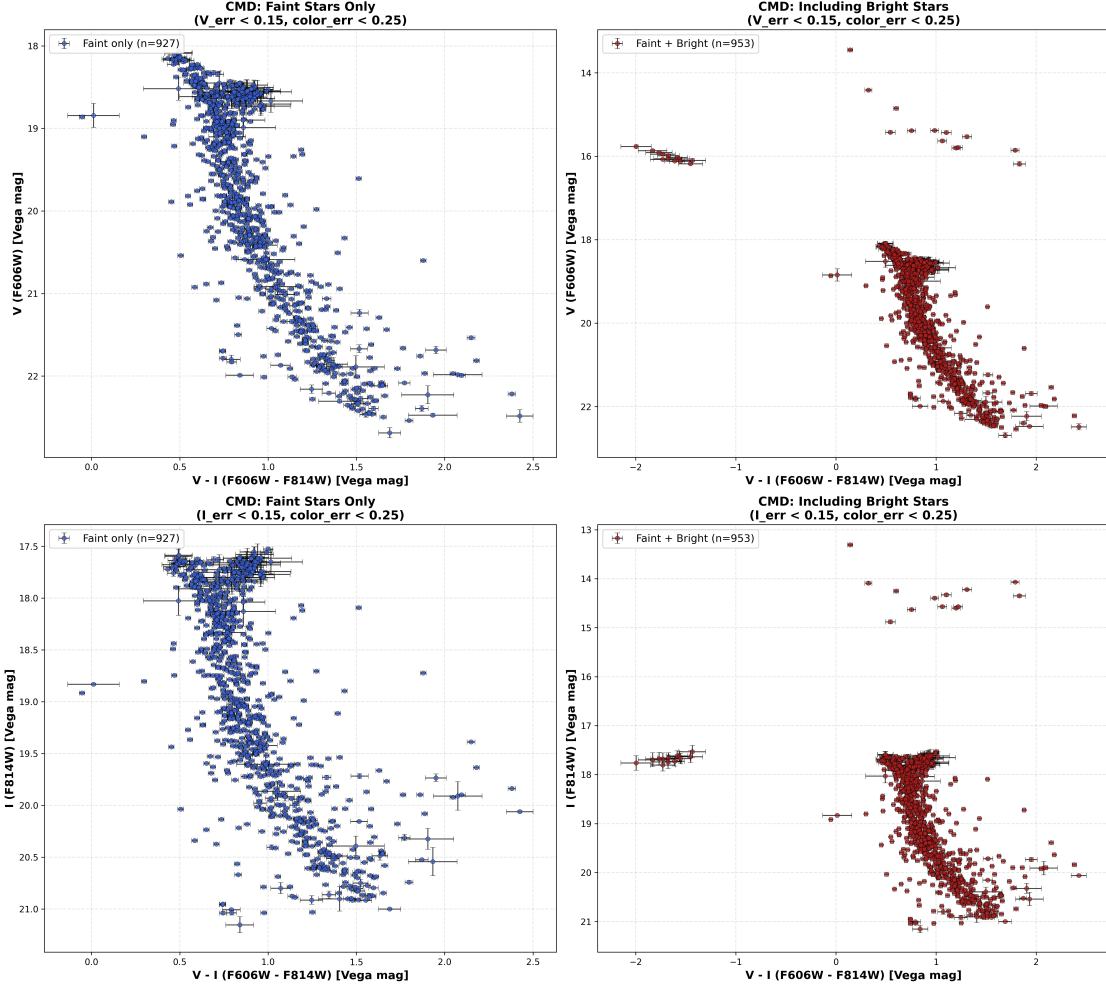


Figure 4: Color–magnitude diagrams before main-sequence fitting. Error bars indicate photometric uncertainties in magnitude and color.

The CMDs reveal the characteristic stellar populations of an old, metal-rich open cluster. A well-defined main sequence extends from the turnoff near $V \approx 19$ mag down to the photometric limit at $V \approx 23$ mag, spanning roughly four magnitudes. The main-sequence turnoff—where stars exhaust hydrogen in their cores and begin evolving toward the giant branch—is visible as the blueward bend of the sequence toward brighter magnitudes.

Above the turnoff, a sparsely populated horizontal branch appears at $V \approx 16$ mag with distinctly blue colors ($(V - I)$ between -1.5 and -2.0 mag), representing core helium-burning stars. Table 3 summarizes the approximate locations of these principal CMD features.

Table 3: Identified CMD Features

Feature	V (mag)	I (mag)	$(V - I)$ (mag)
Main-sequence turnoff	~ 19.0	~ 18.0	[0.6, 0.9]
Main sequence	[19.0, 22.0]	[18.0, 20.5]	[0.5, 1.5]
Horizontal branch	~ 16.0	~ 17.7	[-1.5, -2.0]

The comparison between the left and right panels of figure 4 shows that including bright stars extends the CMD to brighter magnitudes without changing the morphology of the main sequence in the fitting region. The additional scatter at very blue colors ($(V - I) < 0$) in the faint+bright dataset arises from horizontal-branch stars and possible field-star contamination, but these objects lie well outside the main-sequence selection box and do not affect the distance determination.

3.3 Error Analysis and Quality Filtering

Figure 5 shows photometric errors and their relationship to magnitude, motivating our quality cuts. The error histograms (top row) show that the vast majority of stars have photometric uncertainties well below our quality thresholds, with the distributions peaking near 0.02–0.03 mag in both V and I bands. The similarity between the faint-only (blue) and faint+bright (red) distributions confirms that the adaptive-aperture technique achieves comparable precision for bright stars.

The bottom row shows the expected trend of increasing photometric error at fainter magnitudes, following the characteristic $\sigma \propto 10^{0.4m}$ relationship predicted by Poisson statistics. Stars rejected by our quality cuts lie predominantly at the faint end ($V \gg 23$ mag), where signal-to-noise ratios drop below acceptable levels. The quality thresholds of 0.15 mag (individual bands) and 0.25 mag (color) were chosen to retain the majority of the main sequence while excluding sources with uncertainties large enough to broaden the CMD and compromise the ridge-line fitting.

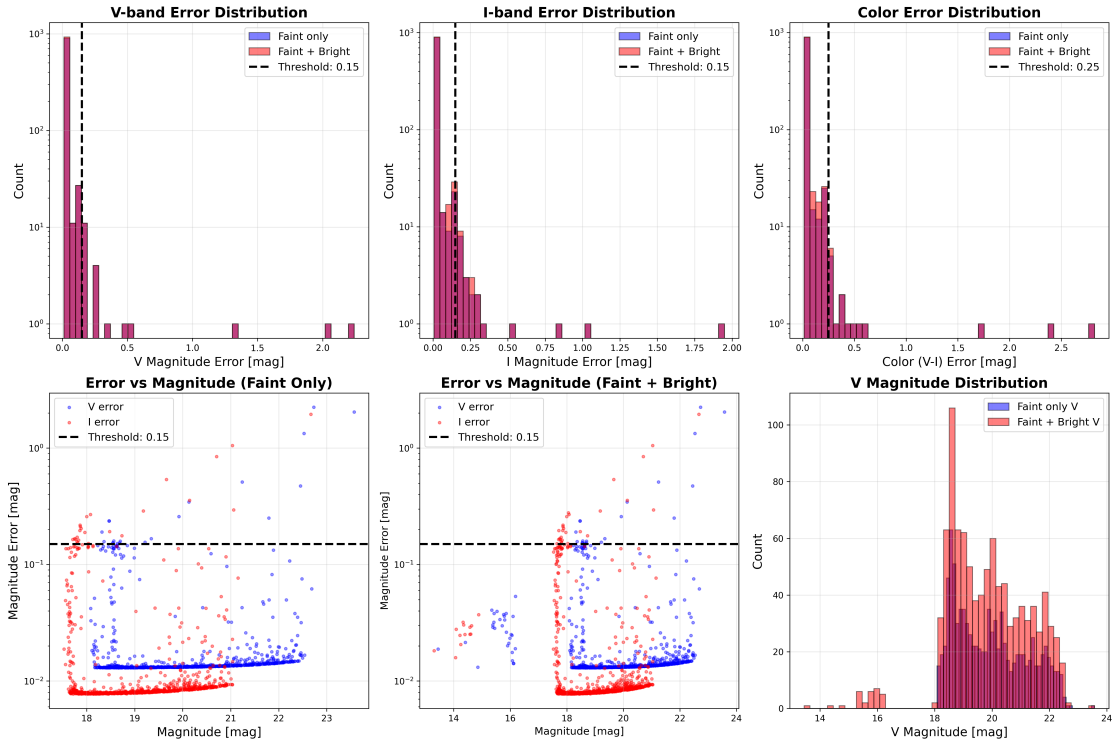


Figure 5: Photometric error analysis. Top row: Histograms of V-band, I-band, and color errors for both faint-only (blue) and faint+bright (red) datasets. Vertical dashed lines indicate quality thresholds. Bottom row: Error as a function of magnitude, showing expected increase at faint magnitudes.

3.4 Main Sequence Identification

We applied the iterative ridge-line fitting procedure to identify main sequence stars and determine the characteristic locus for distance measurement. Table 4 summarizes the fitting parameters and convergence statistics.

The initial selection boxes were defined to encompass the clearly visible main sequence while excluding the turnoff region—where the CMD curves sharply—and the faint limit, where photometric scatter increases. The V-band box spanning

Table 4: Main Sequence Fitting Results

Parameter	V-band	I-band
Selection box magnitude range (mag)	19.0–22.0	18.0–20.5
Selection box color range (mag)	0.5–1.5	0.5–1.5
Stars in initial box	564	613
Iterations to convergence	7	6
Stars rejected (total)	74	64
Final main sequence stars	490	549
Polynomial order	4	4
Bin size (mag)	0.4	0.4
Rejection threshold	3σ	3σ

19.0–22.0 mag captured 564 stars, while the I-band box (18.0–20.5 mag) contained 613 stars, reflecting the different magnitude ranges sampled in each filter for the same stellar population.

The iterative fitting converged rapidly, requiring only 7 iterations for the V-band and 6 for the I-band. In each iteration, progressively fewer stars were rejected as the polynomial ridge line stabilized: the V-band fitting rejected 31 stars in the first iteration, decreasing to just 2 stars by the sixth iteration before converging with no rejections in the seventh. This behavior indicates a well-defined main sequence with a small population of outliers (binary stars, field contaminants, or stars with anomalous photometry) that are efficiently removed by the 3σ clipping procedure.

The final main sequence samples contain 490 stars (V-band, 87% of the initial selection) and 549 stars (I-band, 90%). The slightly higher retention rate in I-band likely reflects the reduced photometric scatter at longer wavelengths and the narrower magnitude range of the selection box. Figure 6 shows the fitting results, with the polynomial ridge line tracing the center of the main sequence distribution.

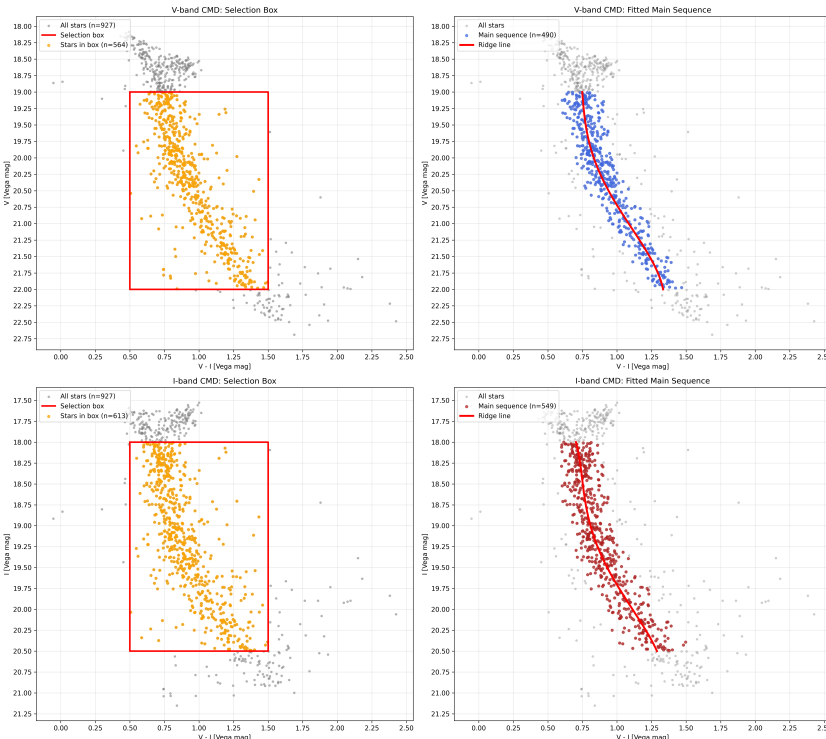


Figure 6: Main sequence fitting results. Left panels: Initial selection box (red rectangle) overlaid on the CMD, with stars inside the box highlighted in orange. Right panels: Final main sequence stars after iterative 3σ clipping, with the fourth-order polynomial ridge line (red curve) defining the main sequence locus. Top row: V-band. Bottom row: I-band.

3.5 Distance Determination

Table 5 lists reference cluster M15 parameters used for comparison.

Table 5: Reference Cluster Parameters (M15)

Parameter	Value	Source
Distance	9.98 ± 0.47 kpc	McNamara et al. (2004)
Distance modulus (μ)	14.996 ± 0.102 mag	Calculated
V magnitude at $(V-I) = 0.8$	22.50 ± 0.25 mag	Houdashelt et al. (2001)
Absolute V magnitude at $(V-I) = 0.8$	7.504 ± 0.270 mag	Calculated

Table 6 summarizes the measured NGC 6791 main sequence at the target color.

Table 6: NGC 6791 Main Sequence Measurements at $(V-I) = 0.8$

Parameter	Value
Target color	0.80 mag
Color tolerance	± 0.05 mag
Stars in measurement region	129
V magnitude range	19.008 – 20.568 mag
Mean V magnitude	19.683 ± 0.410 mag
V magnitude scatter (σ)	0.410 mag
Interpolated ridge V	19.774 ± 0.410 mag
Mean measured color	0.798 ± 0.027 mag

Figure 7 illustrates the stars used to determine the distance modulus.

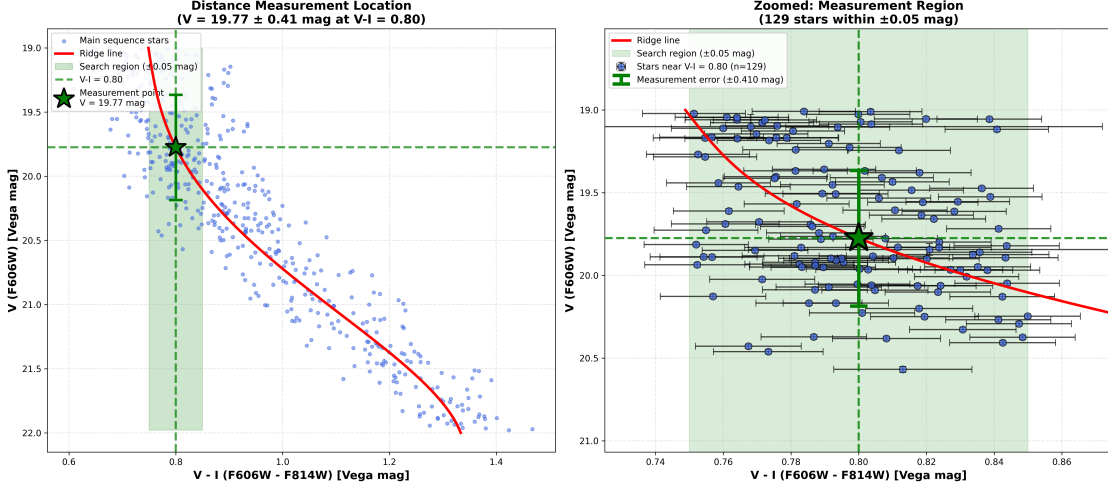


Figure 7: Distance measurement region on the V-band CMD. Left: full CMD with main sequence (blue points), ridge line (red curve), and measurement at $(V-I)=0.8$ (green star). Right: zoom showing individual stars with error bars within the ± 0.05 mag color tolerance.

Finally, Table 7 lists the main contributions to the uncertainty in distance determination.

Table 7: Error Budget for Distance Determination

Error Source	Contribution (mag)	Description
Target V measurement scatter	0.410	Intrinsic width of main sequence at $(V-I) = 0.8$
Reference V magnitude	0.250	Uncertainty from reading published CMD
Reference distance modulus	0.102	Propagated from M15 distance uncertainty
Total (quadrature sum)	0.491	Combined uncertainty in distance modulus

3.6 Comparison: Faint-Only vs Including Bright Stars

Both the faint-only (927 stars) and faint+bright (953 stars) analyses yield identical distance measurements within uncertainties, showing that including the brightest 30 stars does not significantly affect main sequence fitting in the $V = 19\text{--}22$ mag range.

4 Discussion

5 Conclusions

Recommendations for Future Work

5.1 Acknowledgments

5.2 AI Usage

The use of AI (LLMs) was included in this lab report. The main use was for formatting text, tables, and citations. It was also used to check for major typos and grammatical errors. It was not used to explicitly generate text. All information inside the tables was manually checked to ensure it was accurate post formatting.

References

- Nasser M. Ahmed. A comprehensive study of the old open cluster NGC 6791 using Gaia DR3 data and BV photometry. , 543(2):1584–1601, October 2025. doi: 10.1093/mnras/staf1469.
- Annalisa Calamida, Jennifer Mack, Jennifer Medina, Clare Shanahan, Varun Bajaj, and Susana Deustua. New time-dependent WFC3 UVIS inverse sensitivities. Instrument Science Report WFC3 2021-4, 33 pages, February 2021.
- Mark L. Houdashelt, Rosemary F. G. Wyse, and Gerard Gilmore. Hubble Space Telescope Color-Magnitude Data for Globular Clusters. I. Transformations between STIS LP Magnitudes and WFPC2 F606W and F814W Magnitudes. , 113(779):49–65, January 2001. doi: 10.1086/317974.
- B. J. McNamara, T. E. Harrison, and H. Baumgardt. The Dynamical Distance to M15: Estimates of the Cluster’s Age and Mass and of the Absolute Magnitude of Its RR Lyrae Stars. , 602(1):264–270, February 2004. doi: 10.1086/380905.